Nanoscale Advances

ROYAL SOCIETY OF CHEMISTRY

PAPER

View Article Online
View Journal | View Issue

Cite this: *Nanoscale Adv.*, 2021, **3**, 4106

Bi_2O_3 nano-flakes as a cost-effective antibacterial agent

Luke D. Geoffrion, [a] David Medina-Cruz, [b] Matthew Kusper, [a] Sakr Elsaidi, [a] Fumiya Watanabe, [c] Prakash Parajuli, [d] Arturo Ponce, [d] Thang Ba Hoang, [e] Todd Brintlinger, [f] Thomas J. Webster [b] and Grégory Guisbiers *[a]

Bismuth oxide is an important bismuth compound having applications in electronics, photo-catalysis and medicine. At the nanoscale, bismuth oxide experiences a variety of new physico-chemical properties because of its increased surface to volume ratio leading to potentially new applications. In this manuscript, we report for the very first time the synthesis of bismuth oxide (Bi_2O_3) nano-flakes by pulsed laser ablation in liquids without any external assistance (no acoustic, electric field, or magnetic field). The synthesis was performed by irradiating, pure bismuth needles immerged in de-ionized water, at very high fluence ~160 J cm^{-2} in order to be highly selective and only promote the growth of two-dimensional structures. The *x*- and *y*-dimensions of the flakes were around 1 μm in size while their thickness was 47.0 ± 12.7 nm as confirmed by AFM analysis. The flakes were confirmed to be α- and γ-Bi_2O_3 by SAED and Raman spectroscopy. By using this mixture of flakes, we demonstrated that the nanostructures can be used as antimicrobial agents, achieving a complete inhibition of Gram positive (MSRA) and Gram negative bacteria (MDR-EC) at low concentration, ~50 ppm.

Received 30th October 2020
Accepted 4th June 2021

DOI: 10.1039/d0na00910e

rsc.li/nanoscale-advances

1 Introduction

When penicillin was discovered on September 1928 by Sir Alex Fleming, it changed the face of medicine.[1,2] This "miracle drug,", as it was known, was able to offer a cure for some of the most nefarious diseases. It was only in 1942 that penicillin could be produced at an industrial scale and started to really make an impact in people's daily life.[1] However, due to the benefits of this new drug, doctors started prescribing it massively for all sorts of diseases and people started to self-medicate themselves. When antibiotics are overused or used inappropriately (*i.e.*, when a patient does not finish a full course of treatment), it helps in the spread of resistant bacteria. After a course of antibiotics, some naturally resistant bacteria will be left behind, survival-of-the-fittest style; the more frequent antibiotics are used, the more prevalent these fiercer strains will become. According to the World Health Organization, the inappropriate use of antibiotics in animal husbandry is an underlying contributor to the emergence and spreading of antibiotic-resistant germs, and consequently the use of antibiotics as growth promoters in animal feeds should be restricted.[3] Adjacent bacteria can also acquire resistance by mutating or exchanging genetic material with the resistant strains. When those treatment-resistant bacteria grow and multiply, they can lead to new infections that become difficult or even impossible to treat. It has been estimated that by 2050, antibiotic-resistant bugs could kill an estimated 10 million people each year. Bacterial infections arise almost everywhere from drinking water[4,5] to medical implants.[6] An answer to this problem could be found from nanoscience by investigating new morphologies of materials as new antibacterial agents.

Indeed, at the nanoscale, quantum effects and a huge surface to volume ratio are responsible for the new physico-biochemical properties of materials.[7,8] Various materials as noble metals,[9,10] transition elements,[11] alloys,[11,12] carbon-based,[13] or metal-oxides[14–17] have all been investigated for their nano-features. Due to these new properties at the nanoscale, treatments for bacterial infections have been developed. For example, gold (Au)[9] and silver (Ag) nanoparticles (NPs)[10] have been used to this aim and have shown great results. These chemical elements present naturally antimicrobial activity with a low associated cytotoxicity.[18,19] These great results are not without drawbacks. Au and Ag are rare elements with abundances of 0.004 and 0.075 mg kg^{-1} in the Earth's crust,[20]

[a]*Department of Physics & Astronomy, University of Arkansas Little Rock, 2801 South University Avenue, Little Rock, AR 72204, USA. E-mail: gxguisbiers@ualr.edu*

[b]*Department of Chemical Engineering, Northeastern University, 313 Snell Engineering Center, 360 Huntington Avenue, Boston, MA 02115, USA*

[c]*Center for Integrative Nanotechnology Sciences, 2801 South University Avenue, Little Rock, AR 72204, USA*

[d]*Department of Physics & Astronomy, The University of Texas at San Antonio, One UTSA circle, San Antonio, TX 78249, USA*

[e]*Department of Physics & Materials Science, The University of Memphis, Memphis, TN 38152, USA*

[f]*U.S. Naval Research Laboratory, Nanoscale Materials Section, 4555 Overlook Ave SW, Washington, DC 20375, USA*

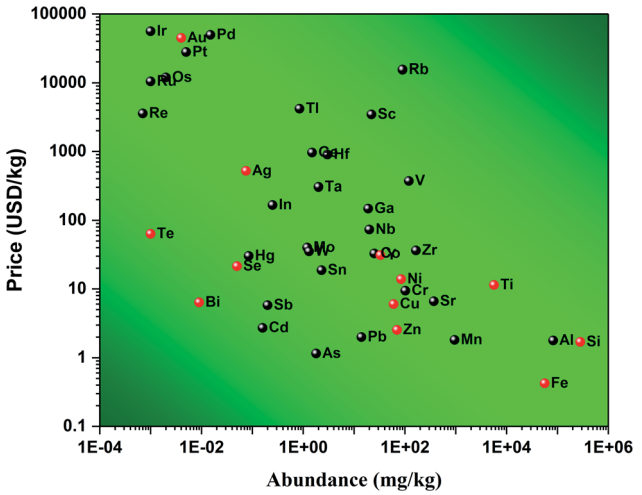

Fig. 1 Price of various chemical elements *versus* their abundance in the Earth's crust. Data were collected from ref. 20. The chemical elements highlighted in red are common elements used for biomedical applications.

Table 1 Bismuth oxide (Bi_2O_3) physico-chemical properties

Phase	Crystal structure	Lattice parameters *a* (A)	*b* (A)	*c* (A)	Energy bandgap (eV)	Applications	Ref.
α	Monoclinic	5.848	8.166	7.510	2.8	Photo-catalysis	38, 29 and 30
β	Tetragonal	7.730	—	5.630	2.5	Water purification, photo-catalysis	39, 29 and 31
γ	b.c.c.	10.268	—	—	1.9	[a]	40
δ	f.c.c.	5.644	—	—	1.7–2.0	Fuel cells, electronics	41 and 44
ω	Triclinic	4.956	5.585	12.730	[a]	[a]	43
ε	Orthorhombic	7.269	8.639	11.970	[a]	[a]	42

[a] Not reported.

respectively. Consequently, their price is around 44 800 and 521 USD per kg,[20] respectively; see Fig. 1. Therefore, any antibacterial treatment based on those expensive chemical elements is not affordable to a large population. This opens the following question: are there any materials achieving similar antibacterial results and being affordable? Some reports have suggested chemical elements such as selenium (Se)[21] and tellurium (Te),[22] and although being cheaper than gold and silver, they are still relatively expensive (21.4 and 63.8 USD per kg).[20] Furthermore, these elements are extensively used in solar cell and electronic industries which keeps their price relatively high for medical applications. That is why the American Physical Society and the Materials Research Society have labelled these elements as Energy Critical Elements.

However, bismuth (Bi) seems to be an element of choice for biomedical applications.[23,24] Many studies have demonstrated its applications in radio-sensing[25] due to their high density which allows for better contrast imaging. When oxidized, bismuth forms bismuth(III) oxide, Bi_2O_3 which is known for its applications in electronics,[26] photo-catalysis,[27–32] medicine,[33,34] gas sensing,[35] water purification,[31] and γ-ray shielding.[36] As a photo-catalyst, Bi_2O_3 has been tested to photodegrade rhodamine B,[30] methyl orange,[27] rhodamine 6D, and other various water pollutants.[31] In medicine, α-Bi_2O_3 coated with (3-aminopropyl)trimethoxysilane and methotrexate were shown to enhance radio-sensitizing features in dose enhancement radiation therapy.[34] It was shown by Stewart *et al.*[33] that α-Bi_2O_3 NPs have high radio-sensitizing capacity. Additionally, it was also shown that Bi_2O_3 is biocompatible.[37] Besides those properties, Bi_2O_3 is a p-type semiconductor and polymorph material that exhibits six different crystal phases: α is monoclinic,[38] β is tetragonal,[39] γ is body-centered cubic,[40] δ is face-centered cubic,[41] ε is orthorhombic,[42] and ω is triclinic.[43] Each of these crystalline phases exhibits very distinct physico-chemical properties that allow for different potential applications, see Table 1. At room temperature, the most stable and common crystalline phase for Bi_2O_3 is the α-phase.

Several methods have been proposed to synthesize Bi_2O_3 nanostructures of various sizes and shapes. These methods include: oxidative metal vapor transport deposition,[45] sol–gel methods,[46,47] wet-chemical synthesis,[48] and pulsed laser ablation in liquids (PLAL).[14–17,23,24,49] Of these methods, PLAL is the most non-equilibrium thermodynamic manufacturing process. Due to this, nanostructures produced by PLAL are influenced by a large number of parameters ranging from the type of target to the fluence of the laser.[50] Most PLAL studies on Bi_2O_3 nanomaterials have been performed using lasers operating at low laser repetition rates and low laser fluence; consequently, spherical NPs were synthesized;[14–17,23,24,51–53] see Table 2. Only one PLAL study, completed by Rosa *et al.*,[52] was done at a higher repetition rate of 1.5 kHz with an ablation time of 2 minutes. It is the only study that has been completed at a high repetition rate, but the authors did not report the laser fluence or the power of the laser. The laser repetition rate strongly influences the final size and shape of the nanostructures due to the re-irradiation of the nanostructures floating within the colloidal solution during the synthesis.[54] Those multiple irradiations induce fragmentation of the particles already produced by crossing the beam multiple times after their initial synthesis. By increasing the repetition rate, the concentration of particles within the solution also increases until the repetition rate is fast enough that the beam starts hitting the cavitation bubble formed during the previous irradiation.[55] Another important parameter to consider is the target.[54] Indeed, the initial starting shape of the target (powder or pellets) also influences the final size of the NPs.[56] Pellets undergo an ablation process while a powder undergo mainly a fragmentation process.

Most recently, Dadashi *et al.*[23] was able to combine PLAL of Bi-based-NP with a post process treatment coating them with gold for biomedical applications. Another recently published

Table 2 Bismuth oxide (Bi_2O_3) nanostructures by PLAL

	Laser parameters					Target parameters				
Group	Laser type	f (Hz)	τ (ns)	t (min)	F (J cm^{-2})	Target type	Liquid	V (ml)	Products	Ref.
Escobar-Alarcon	355 nm Nd:YAG	10	5	10	0.6–1.1	99.99% purity Bi disk	DI H_2O	[b]	α-Bi_2O_3 NPs α,β-Bi_2O_3 NSs	15
Gondal	355 nm Nd:YAG	[b]	[b]	40	[b]	99.998% purity Bi Powder	H_2O_2	10	α-Bi_2O_3 NPs	16
Dadashi	1064 nm Nd:YAG	10	12	5	118 mJ per pulse[a]	99.99% purity	DI H_2O	60	α,β-Bi_2O_3 NPs	14
Ismail	1064 nm Nd:YAG	1	[b]	200	12	99.99% purity Bi	DI H_2O	[b]	α-Bi_2O_3 NPs	17
Rosa	1064 nm Nd:YAG	1500	200	2	[b]	99.999% purity Bi pellets	DI H_2O	4	Bi NPs	52
This work	1064 nm Nd:YAG	1000	100	5	160	99.97% purity Bi rods	DI H_2O	7	Bi_2O_3 NFs	

[a] Given as energy per pulse. [b] Not reported.

PLAL study detailed a new type of synthesis protocol called Sonication assisted-PLAL (S-PLAL); where without sonication the group was able to synthesize Bi_2O_3 nanoparticles, while with sonication (S-PLAL) they were able to synthesize Bi_2O_3 nanosheets.[15]

To the best of our knowledge, this paper presents for the first time the synthesis of Bi_2O_3 nano-flakes (Bi_2O_3 NFs) by PLAL without any external field assistance (no acoustic, electric or magnetic field). This work includes characterization of these nano-flakes by Atomic Emission Spectroscopy (AES), Transmission Electron Microscopy (TEM) with Energy Dispersive Spectroscopy (EDS), Selected Area Electron Diffraction (SAED), X-ray Photoemission Spectroscopy (XPS), Atomic Force Microscopy (AFM), Scanning Electron Microscopy (SEM), and Raman Spectroscopy. After complete characterization, the nanostructures have been tested for their biomedical applications as antibacterial agents, towards both Gram-negative and -positive antibiotic-resistant strains.

2 Materials and methods

2.1 Synthesis of Bi_2O_3 NFs

A single bismuth needle of 99.97% purity from Alfa Aesar [LOT: N27E043] was placed at the bottom of a flat cylindrical beaker (Pyrex) and was covered with 7 mL of molecular biology grade de-ionized water (DI H_2O) from Alfa Aesar [LOT: 177910]. The needle was then irradiated by a Q-Switched Nd:YAG laser from Electro Scientific Industries emitting in the infrared region at 1064 nm. The laser beam was reflected by a flat mirror angled at 45° with respect to the laser rail and then directed through an 83 mm lens which focused the beam onto the bismuth needle submerged in DI water. The beam size diameter at the surface of the target was measured to be around 100 μm. The laser power was measured in continuous mode to be 12.5 W. This gives a fluence of ~160 J cm^{-2}. The irradiation lasted for 5 minutes at a repetition rate of 1 kHz. The laser beam was hitting the same spot on the target during the entire duration of synthesis. After irradiation, the target (bismuth needle) was removed from the solution, which was dark brown in color, and a tiny dark spot was observed at the surface of the needle revealing the presence of the ablation crater. All samples were prepared for analysis just after the synthesis was completed.

2.2 Material characterization

After irradiation, the solution was poured into a 5 mL opaque plastic microtube for storage and further analysis. The solution was first analyzed by AES (AES, MP-4210 from Agilent). A droplet of the colloidal solution was then placed onto a silicon wafer for SEM analysis within a JEOL JSM7000F microscope. AFM (Bruker Icon AFM) was performed in tapping mode using a silicon AFM probe from Ted Pella, Inc [Prod No. TAP300-G-10] with a resonant frequency of 300 kHz and a force constant of 40 N m^{-1}. A droplet was placed onto a carbon film copper grid for analysis by TEM performed in the JEOL JEM2100F and the JEOL ARM200F microscopes operated at 80 kV and 200 kV, respectively. The crystalline structure has been analyzed by SAED patterns. Off-axis electron holography has been performed to determine the thickness of the samples and compared with AFM measurements. In the optical measurement procedure (Raman spectroscopy), nano-flakes were first drop-casted onto a Si substrate. The sample was optically excited by an ultrafast laser (Coherent Chameleon Ultra II, 80 MHz, 150 fs) by a 633 nm continuous wave laser for Raman detection. The excitation spot and average power were 0.42 μm/1 mW for 633 nm laser, respectively. The Raman signal was filtered by appropriate long-pass filters, analyzed by a spectrometer (Horiba iHR550) and detected by a Charged-Coupled Device (CCD) camera. For XPS measurements, a drop of colloidal solution was placed onto a silicon wafer and then processed into a Thermo K-Alpha XPS.

2.3 Biomedical characterization

Two different strains of bacteria were tested for antimicrobial properties using the Bi_2O_3 NF: one Gram-negative bacteria (multidrug-resistant *Escherichia coli* (MDR-EC) (ATCC BAA-2471; ATCC, Manassas, VA)) and one Gram-Positive bacteria (Methicillin-resistant *Staphylococcus aureus* (MRSA) (ATCC 4330; ATCC, Manassas, VA)) were utilized for the antibacterial tests. The cultures were kept on agar plates at 4 °C.

Colony counting unit assays were completed by seeding the bacteria in a 96-well plate mixed with different concentrations of Bi_2O_3 NF. The plates were incubated at 37 °C for 8 h; after that period of time, they were removed from the incubator and diluted with PBS in a series of vials by $\times 10^4$ $\times 10^5$ and $\times 10^6$. Three drops of 10 μL were taken of each dilution and deposited

on an LB agar plate. The plates were deposited inside an incubator at 37 °C until the colonies grew enough without reaching confluency. Afterward, the numbers of colonies formed were counted, and the data was processed.

All biological experiments were repeated in triplicate ($n = 3$) to ensure the reliability of the results. Statistical significance was assessed using Student's t tests, with a $p < 0.05$ being statistically significant. Results are displayed as mean ± standard deviation.

3 Results

3.1 Effect of laser fluence on morphology

In order to better understand the effect of the laser fluence on the production of nanostructures by PLAL, a series of syntheses were completed at ~30, ~100, and ~160 J cm^2; see Fig. 2a, b and c, respectively. From the SEM images, it is clear that at low laser fluence (Fig. 2a), a mixture of nano-spheres and nano-flakes were synthesized. As the laser fluence was increased, Fig. 2b and c, the spherical population was removed from solution and the nano-flakes were the only population observed. Besides the elimination of nano-spheres, another effect was noticed, in that the nano-flakes morphology became well defined as small squares. This morphology is totally unusual for the PLAL synthesis technique. Consequently, the nano-flakes synthesized at ~160 J cm^{-2} were selected as the focus of the paper.

3.2 Physico-chemical characterization

In order to determine the morphology and chemical nature of the structures within the colloidal solution, TEM and additional SEM were performed. Fig. 3a and b, show low magnification TEM and SEM images of the structures after being drop-casted onto a copper grid and silicon wafer, respectively. From these observations, the "flake" morphology is determined. Fig. 3c shows a typical STEM image of the bismuth-based flakes. EDS was performed in order to identify the chemical nature of the flake. From the EDS analysis, the flake is made of bismuth and oxygen, as expected from the ablation process. Fig. 3d–f show the mapping of bismuth, oxygen, and bismuth plus oxygen, respectively. Bismuth and oxygen can combine according various stoichiometric ratio (1 : 1, 2 : 3, 2 : 5), so to confirm the exact stoichiometric ratio of the bismuth oxide flakes obtained by PLAL, XPS was performed (Fig. 3g and h). The Bi4f7 scan revealed a peak centered about 159 eV which has been attributed to the Bi–O bond corresponding to Bi_2O_3. The Bi4f5 scan revealed a peak centered about 165 eV which is also a peak that has been attributed to the Bi–O bond corresponding to Bi_2O_3. There are no peaks centered about 157 eV or 162 eV which are attributed to the Bi–Bi bond.[57] In Fig. 3f, there is another peak centered on ~531 eV which is commonly attributed to metal oxides. This further confirms the 2 : 3 stoichiometric ratio of our flakes. So clearly, Bi_2O_3 is the material compound constituting the surface of the flakes.

Raman spectroscopy was performed and confirmed the presence of α- and γ-phases of Bi_2O_3 (Fig. 3i). Fig. 3i displays the Raman spectra from several Bi_2O_3 nano-flakes at room temperature. These nano-flakes exhibited several distinguishable Raman peaks which were identified as α-Bi_2O_3 (123, 141, 154, 186, 213, 278, 315, 411 and 450 cm^{-1}) and of γ-Bi_2O_3 (163 and 249 cm^{-1}). From the Raman spectra, α-Bi_2O_3 peaks dominate as reported previously.[58,59] Due to the limitation of the long-pass filter, only the Raman peaks showing up wavenumbers higher than 100 cm^{-1} could be detected. The 123 cm^{-1} mode is coming from A_g symmetry caused by mainly

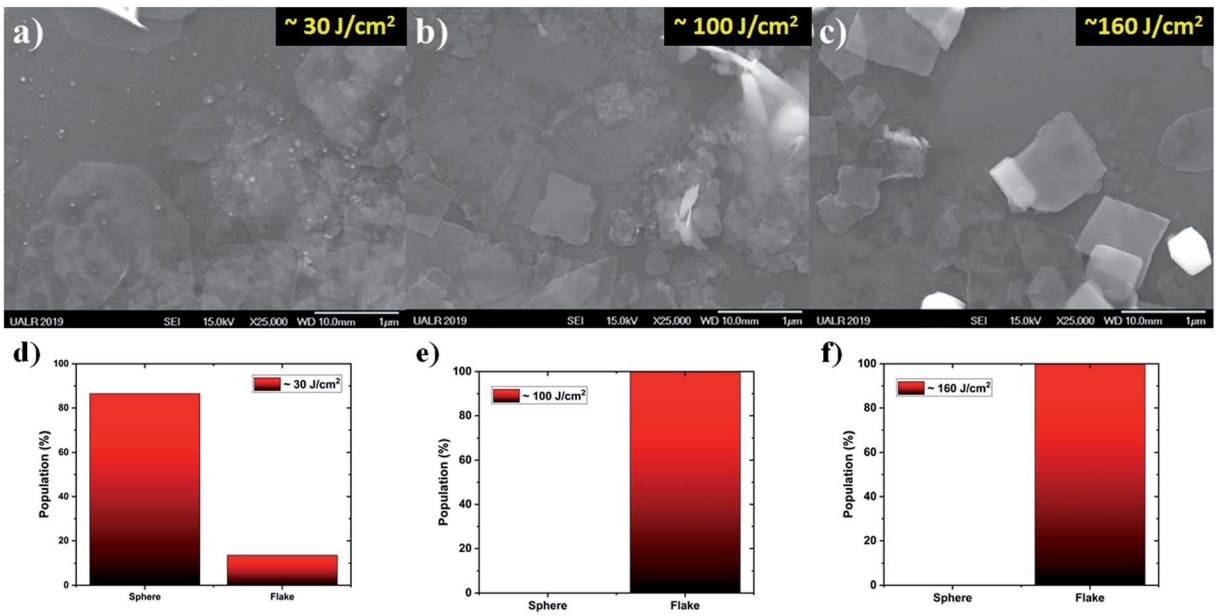

Fig. 2 Effect of laser fluence on the morphology of nanostructures by PLAL ~30 J cm^{-2}, ~100 J cm^{-2}, and ~160 J cm^2; (a), (b) and (c), respectively, and distributions of morphologies for each fluence in (d), (e) and (f), respectively.

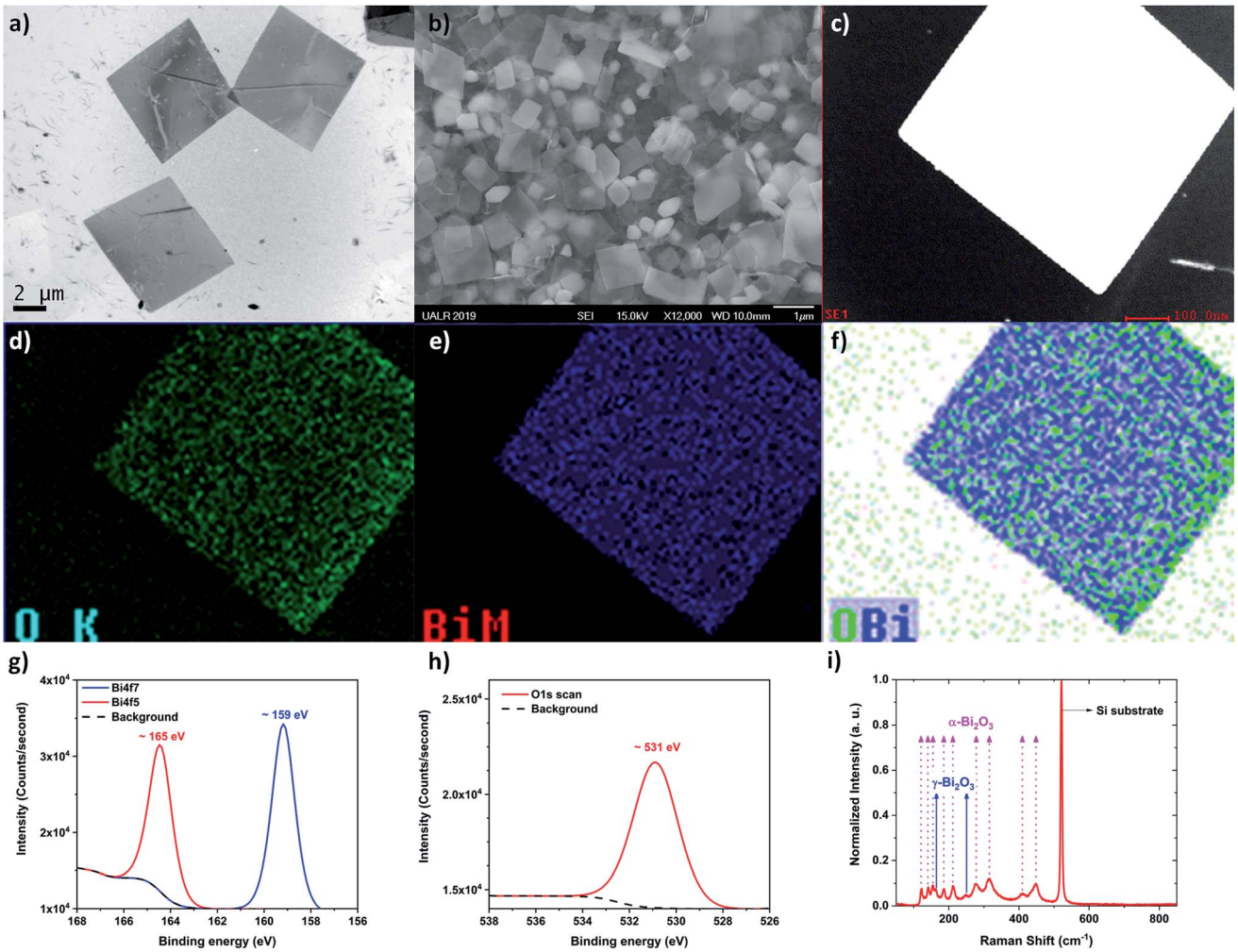

Fig. 3 Bismuth oxide flakes obtained at high fluence (~160 J cm^{-2}) (a) Low-magnification TEM image acquired by using the JEOL JEM2100F at 80 kV. (b) Low magnification SEM image acquired by using the JEOL JSM7000F at 15 kV. (c) Typical STEM image of a flake, (d) oxygen chemical mapping on the flake, (e) bismuth mapping on the flake, and (f) chemical mapping displaying the bismuth and oxygen mapping together. The TEM used to acquire those images was the JEOL JEM2100F at 80 kV, (g) XPS spectra display the bismuth peaks Bi4f7 and Bi4f5 scan, (h) XPS spectra displaying the oxygen peak, (i) Raman spectra confirming that two crystalline phases of bismuth oxide (α and γ, see texts for details) are produced during the PLAL synthesis.

the Bi atoms' participation. Modes of 141 (A_g) and 154 cm^{-1} (B_g) may come from the displacements of both Bi and O atoms in the α-Bi_2O_3 lattice. The Raman peaks of the higher frequency modes 186, 213, 278, 315, 411, 450 cm^{-1} are attributed to the displacements of the O atoms in α-Bi_2O_3.[60]

The chemical composition of the surface of the flakes performed by XPS confirmed the formation of Bi_2O_3, and a mixture of α- and γ-phases were indicated by Raman spectroscopy; however, further studies were necessary in order to determine the crystallinity of the flakes. Indeed, Bi_2O_3 has six different allotropes and they each have their own distinct physico-chemical properties (Table 2). To determine the phase of bismuth oxide synthesized by PLAL, SAED was performed (Fig. 4). From Fig. 4b, the indexed SAED pattern corresponds to the α-Bi_2O_3 phase. Moreover, γ-Bi_2O_3 phase commensurate structures have also been found (Fig. 4c and d).[61,62] The crystalline phases experimentally determined by electron diffraction is performed by finding the zone axis, and subsequently by measuring the reflections of the electron diffraction pattern, and by comparing the distances of the reciprocal lattice of the possible phases. However, despite the consideration of forbidden reflections produced by dynamical interaction, when some reflections (typically weak spots) do not correspond with the expected Bragg diffraction spots and when a simple fraction of the periodic arrangement is identified, *i.e.* (1/2,0,0); then, the atomic distribution can present commensurability. In the analysis performed by electron diffraction, commensurate structures of the γ-phase is measured and shown in Fig. 4c and d. Commensurability has already been observed in Bi_2O_3 by Zhou *et al.*[62] Fig. 4e shows a high resolution TEM (HRTEM) image in which the fast Fourier transform present a commensurate pattern as can be observed in the modulation contrast of the dark field image in Fig. 4f.

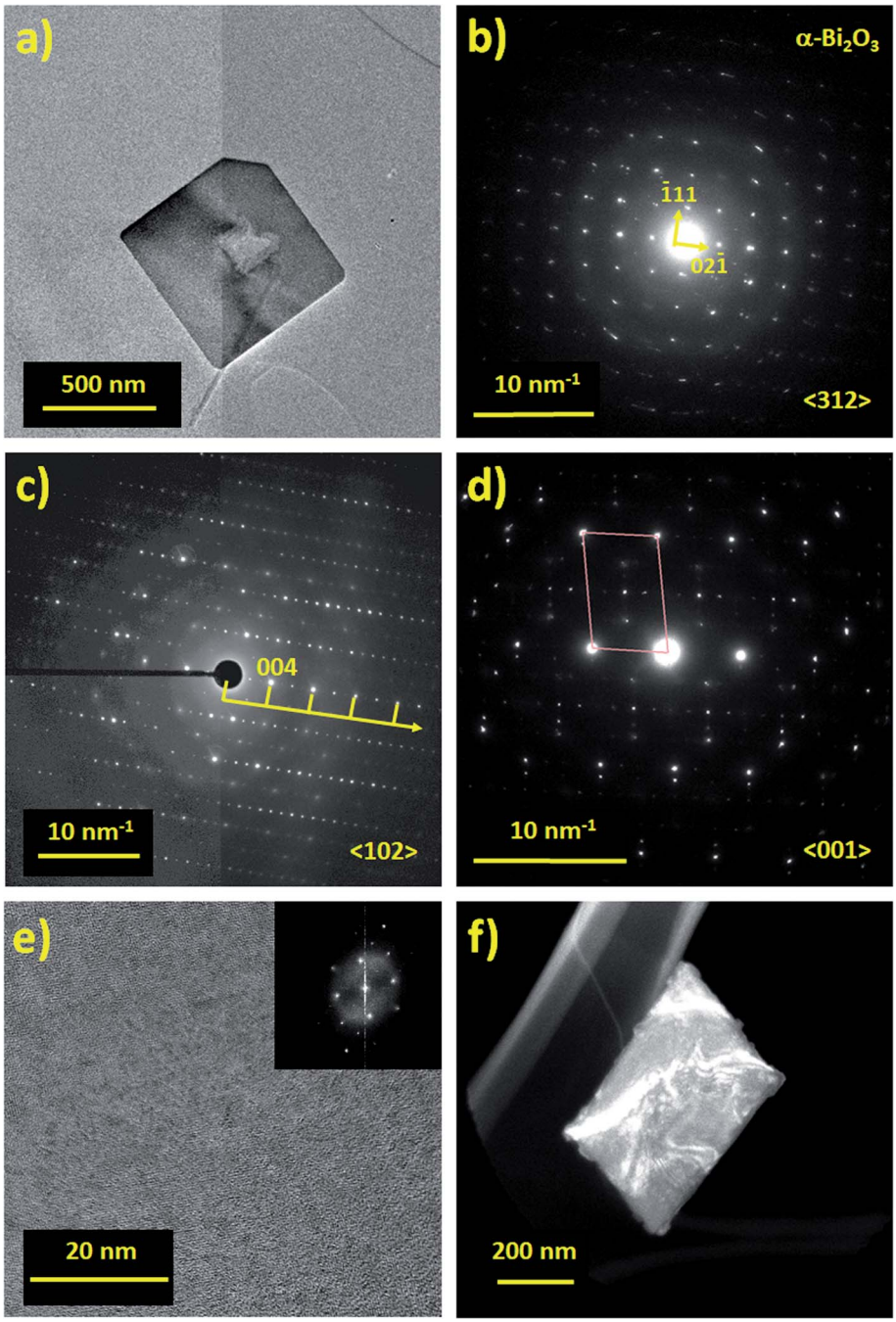

Fig. 4 Bismuth oxide flake obtained at high fluence (~160 J cm^{-2}) (a) TEM image of an α-Bi_2O_3 nano-flake acquired by using the JEOL ARM200F at 200 kV and (b) its SAED pattern taken near the ⟨312⟩ zone axis. (c) and (d) commensurate structures of the γ-Bi_2O_3 nano-flake recorded in two different zone axes, (e) HRTEM image of the commensurate γ-Bi_2O_3 structure and (f) dark field image modulation contrast image.

For thickness determination of the flakes by electron holography, a field of view of 4 microns at 42 V of the bi-prism excitation was used with a fringe contrast of about 25%. Fig. 5a and b show the hologram and the reconstructed phase, respectively. Reconstructed phase of the hologram indicates a phase shift ($\Delta\varphi$) related to the thickness (τ), which is calculated using $\Delta\varphi = C_E|V_0|\tau$, where V_0 represents the mean inner potential for α-Bi_2O_3 (9.35 V), calculated using the atomic scattering amplitudes from ref. 63, and the parameter C_E is 0.00729 rad V^{-1} nm^{-1} for the 200 kV accelerating voltage. Thickness measured by electron holography, after carbon background subtraction (~20 nm of a lacey carbon commercial grid) was ~68 nm as shown in Fig. 5c. Since our average thickness is below 100 nm as confirmed by electron holography, those structures are nano-flakes.

To be complete, AFM measurements were performed to determine more precisely the size distribution of the flakes; see Fig. 6a and b. The additional analysis shows that the heights of

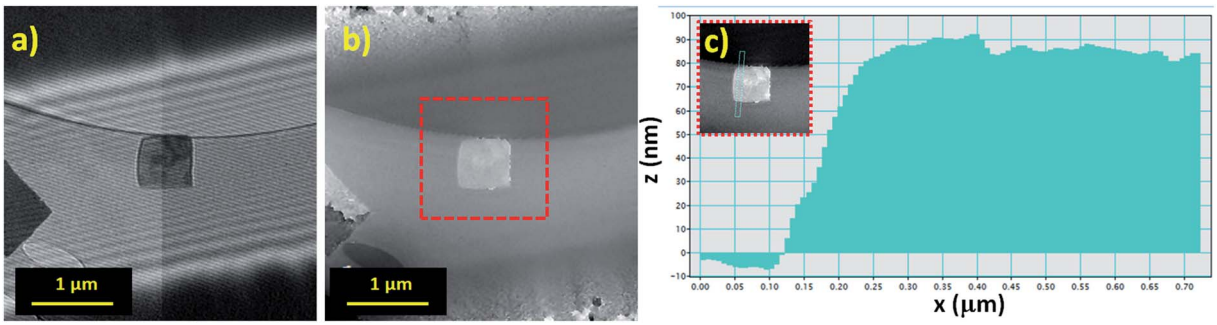

Fig. 5 Thickness determination by off-axis electron holography performed with the JEOL ARM200F at 200 kV: (a) electron hologram, (b) reconstructed phase and (c) thickness intensity profile after carbon background subtraction ~68 nm.

the flakes produced ranged from ~20 nm to ~70 nm, which supports the initial analysis; see Fig. 6c. It is also found that the length and widths of the flakes range from 0.6–1.7 μm and 0.5–1.4 μm, respectively; see Fig. 6d. For surface area and volume determination (Fig. 6e and f), it is assumed that the flakes adopt a rectangular prism morphology which seems to be a good approximation. This allows us to see that the flakes have high surface area and very high volume which results in a fairly low surface to volume ratio. Furthermore, descriptive statistics on the samples were determined and are tabulated in Table 3.

3.3 Antimicrobial assays

Colony counting assays are performed using one Gram-positive, MRSA, and one Gram-negative, MDR-EC. The results presented in Fig. 7 highlight the different responses between each type of bacteria and the Bi_2O_3 NFs. By comparison, the Bi_2O_3 NFs showed the strongest antibacterial effect on the Gram-negative bacteria.

Then, the minimum inhibitory concentration (MIC) was estimated between 0–5 ppm and 5–10 ppm Bi_2O_3 NF's for the Gram-negative and -positive bacteria, respectively. This demonstrates that the Bi_2O_3 NF's are more effective at inhibiting the growth of Gram-negative bacteria. These reported MIC values are significantly lower than those reported in literature by Campos *et. al.* who reported a MIC value of 267 ppm when exposing bismuth oxide NPs to *Escherichia coli* and *Staphylococcus aureus*.[64] The small MIC values obtained in our study can be explained by the "naked" surface of the nanoflakes produced by PLAL. Indeed, the surface of the nanoflakes produced by PLAL is not covered by any surfactants or left-over from chemical reactions, subsequently directly exposing the heavy metal bismuth to the bacteria's membrane. Moreover, the flake morphology (Table 3) also helped to wrap the bacteria; consequently affecting its permeability by modifying the transport through the membrane. Indeed, the spherical cells of *S. aureus* are up to 0.5 μm in diameter while the cells of *E. coli* are cylindrical with 1.0–2.0 μm long and about 0.5 μm in diameter.

A SEM investigation has been performed in order to visualize the interaction between each bacteria and the Bi_2O_3 NFs (Fig. 8). SEM images of control MDR-EC and MRSA (Fig. 8a and c) and bacteria after treatment with a concentration of 25 ppm of Bi_2O_3 NFs (Fig. 8b and d) are shown. The characterization indicates that the treatment with the nanostructures induced changes on both bacterial strains. Disruption of the outer cell membrane and cell lysis was seen after the treatment with the NFs. Therefore, evident cell damage was observed, with an abundant presence of holes and cracks all over the cell membrane, and bacterial deformation and collapse. The cell membrane damage is commonly found to be a consequence of an increased ROS production. From the SEM images of the bacteria, first, there is attachment of the NFs to the bacteria; second, the adhesion is responsible of the bacteria's membrane damage occurring by disrupting the transport of nutrients through the membrane.

Finally, these experimental results are in agreement with the fact that Bi_2O_3 NFs can inhibit the growth of drug resistant pathogens,[65] and this article successfully reports for the first time, the inhibition of the antibiotic resistant pathogens such as MDR-EC and MRSA.

3.4 Cytotoxicity

To determine the cytotoxicity of the Bi_2O_3 NFs on mammalian cells, *in vitro* MTS assays were performed with Human Dermal Fibroblasts (HDF) cells using different nano-flake concentrations, ranging from 10 and 50 ppm for between 24 and 72 hours (Fig. 9). As shown in Fig. 9, no significant cytotoxicity towards HDF cells was found for the whole range of concentrations at 24 h, showing no statistical differences compared to the control. Furthermore, a 72 h treatment led to the same cytotoxicity trend, except for the highest concentration, were there was a slight deviation compared to the control, indicating that such treatment conditions might not be the best option for a 72 h cell exposure.

4 Discussion

4.1 Nano-flake formation mechanism

Now that the 2D structure of the nanostructures has been established, it is important to understand their growth process. Laser exfoliation of the target was considered as a possible growth mechanism, but due to the chemical nature of the flake, Bi_2O_3, the formation of bismuth oxide cannot be explained by exfoliation (*i.e.* exfoliation of a pure bismuth target should result in pure bismuth nano-flakes, not Bi_2O_3 nano-flakes).[66] Therefore, another growth mechanism was considered.[67] PLAL

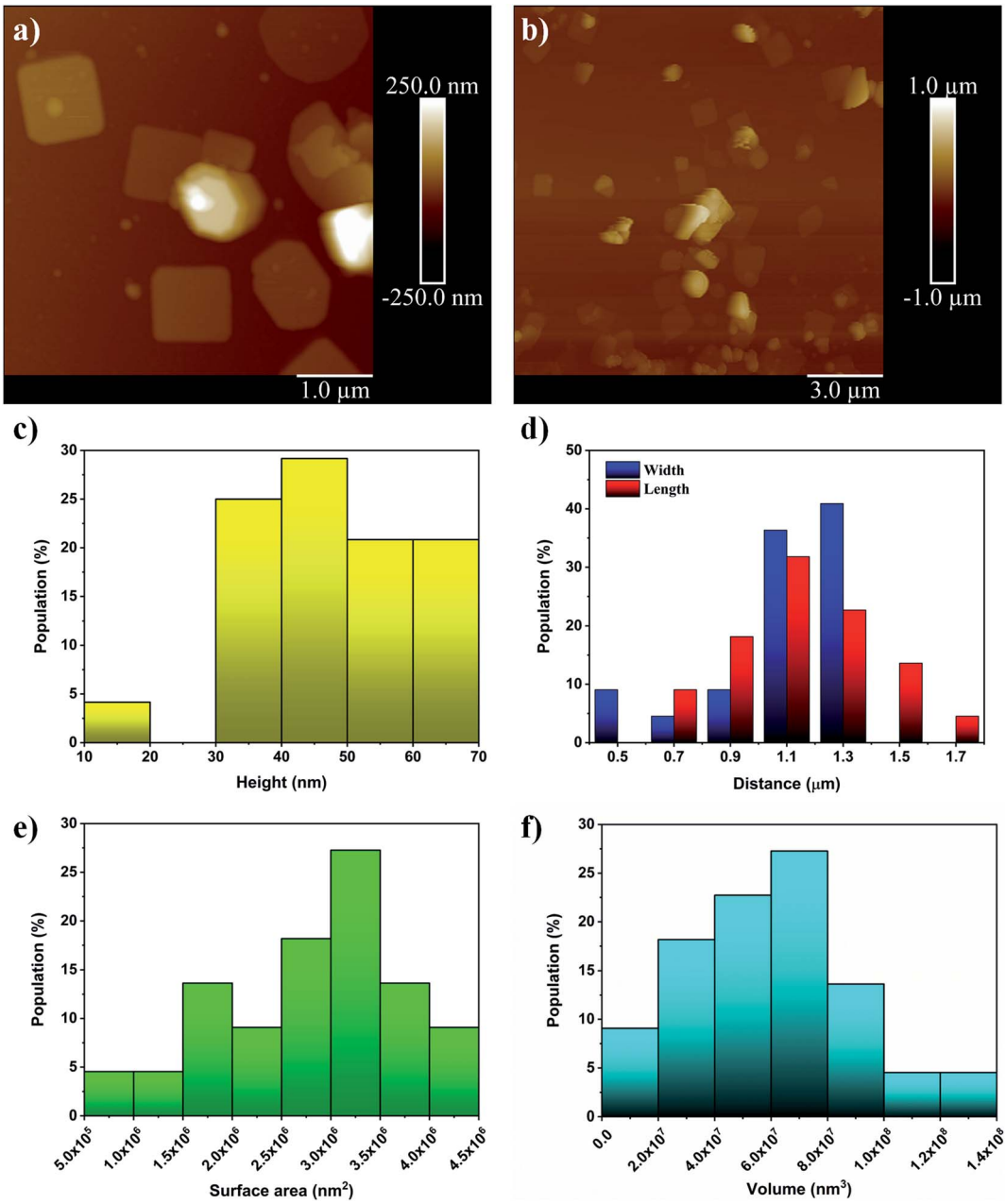

Fig. 6 (a) and (b) are AFM images with scale bars of 1 μm and 3 μm, respectively. (c) and (d) show the distribution of the heights, lengths and widths of the nanoflakes, respectively. (e) and (f) show the surface area and volume distributions, respectively, which are calculated by approximating the morphology of the flakes as rectangular prisms.

is a straightforward physical technique to produce nanostructures. The laser beam interacts with the pure bismuth target while it is submerged in DI water. The target and the solvent get ionized and it consequently creates a plasma made of electrons, bismuth ions, hydrogen ions, and oxygen ions. Then, when the beam is off, the plasma cools down and releases

Table 3 Descriptive statistics for the height, length, width, surface area, volume, and surface to volume ratio of Bi_2O_3 NFs ($n = 22$) as determined by AFM analysis. Values are reported as their average ± standard deviation

Height (nm)	Length (μm)	Width (μm)	Surface area (nm^2)	Volume (nm^3)	Surface to volume ratio (nm^{-1})
46 ± 13	1.15 ± 0.22	1.09 ± 0.25	$(2.8 \pm 0.9) \times 10^6$	$(6.1 \pm 2.9) \times 10^7$	0.05 ± 0.02

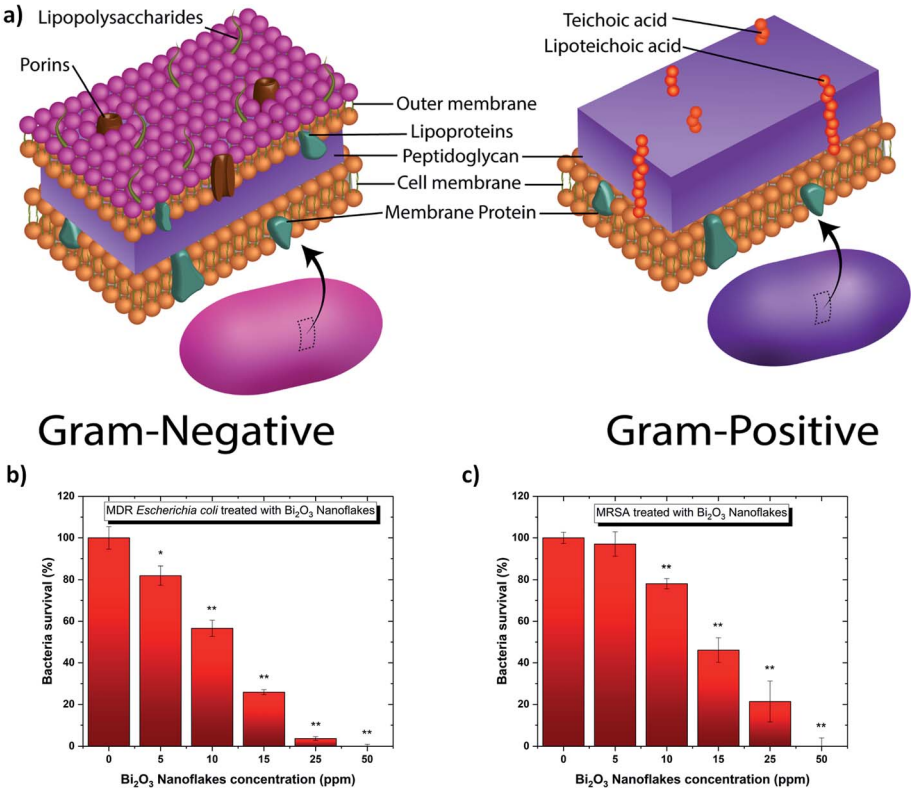

Fig. 7 (a) Artistic representation showing the internal structure of Gram-negative and Gram-positive bacteria. Colony counting assay of (b) MDR-EC and (c) MRSA for 8 h in the presence of different concentrations of Bi_2O_3 NFs. All values represent the mean ± standard deviation. *$p < 0.05$, **$p < 0.01$ (compared to controls).

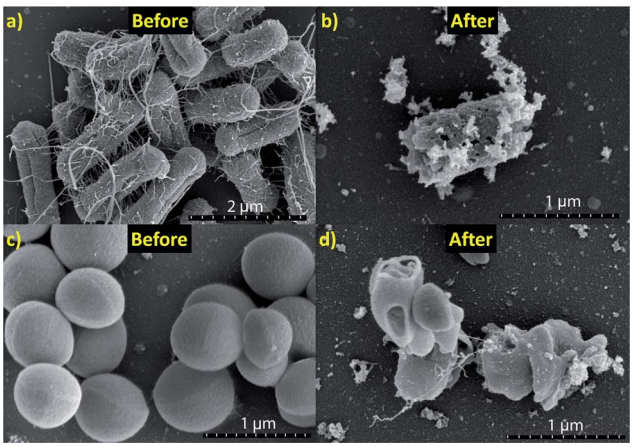

Fig. 8 SEM images of the bacteria before and after interacting with the Bi_2O_3 NFs. (a) MDR-EC before interaction (control). (b) MDR-EC after interaction. (c) MRSA before interaction (control). (d) MRSA after interaction.

the heat to the surrounding solvent creating a cavitation bubble. Within this cavitation bubble, the ions start reacting together forming bismuth oxide compounds. Bismuth oxide adopts a 2D growth in order to minimize the energy of its overall structure by privileging the growth of low surface energy facets.[68] In this case, there are two competing factors, one geometric that minimizes the surface to volume ratio and one energetic that minimizes the surface energy. When the surface energy of the compound is below the surface energy of the solvent then the

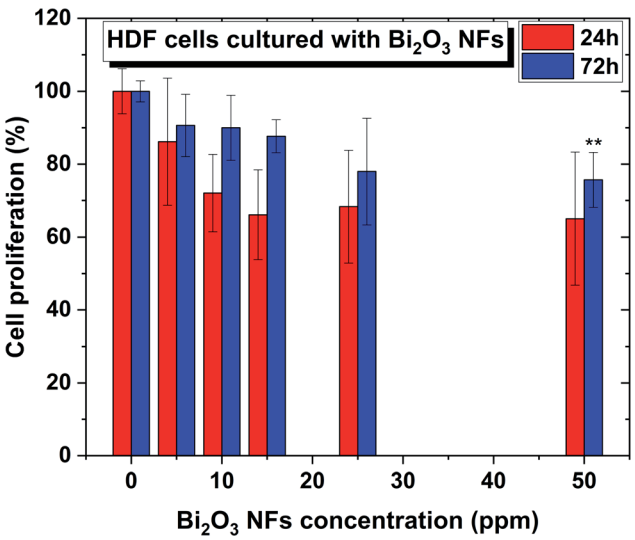

Fig. 9 Human Dermal Fibroblasts (HDF) cells in the presence of Bi_2O_3 NFs at concentrations ranging from 0 to 50 ppm. $n = 3$. All values represent the mean ± standard deviation. *$p < 0.05$, **$p < 0.01$ (compared to controls).

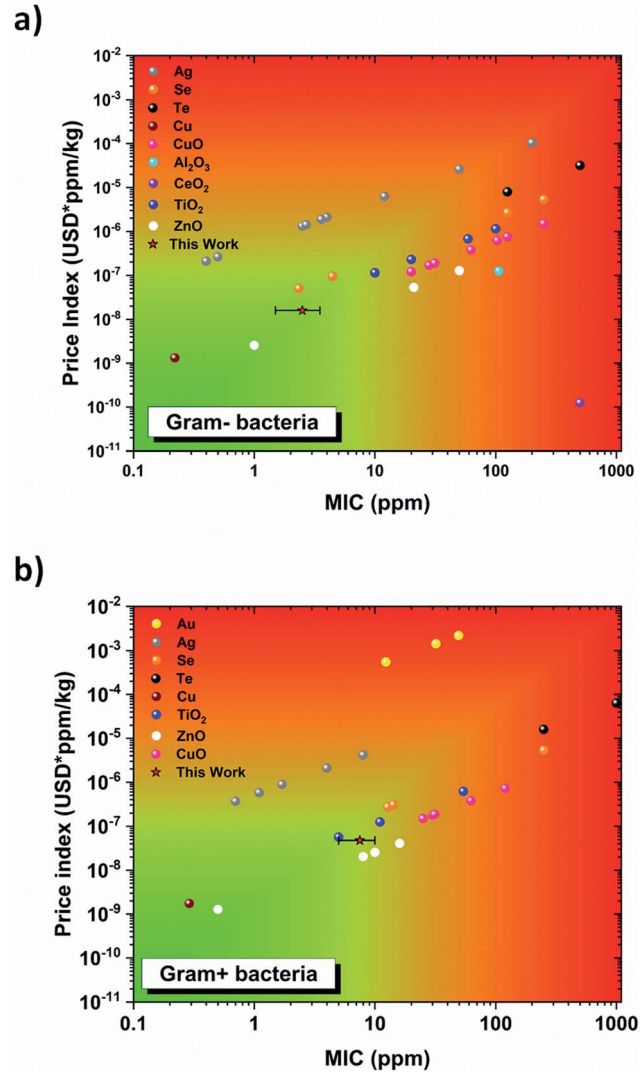

Fig. 10 Cost analysis for various antibacterial materials currently used as nanoparticle treatments. The price index is the price of the material per kilogram multiplied by the MIC *i.e.*, the cost of the treatment. Data were collected from ref. 21, 22, 71–79. (a) It shows the antibacterial cost analysis for Gram-negative bacteria. (b) It shows the antibacterial cost analysis for Gram-positive bacteria.

energetic factor wins and it allows the structure to grow like a 2D material, and when the surface energy of the compound is above that of the solvent, the structure adopts a spherical morphology in order to minimize the surface to volume ratio. The surface energy of Bi_2O_3 was recently measured by the Zisman method (*i.e.* the surface energy of the solid is the surface energy at which a liquid just completely wets the solid) to be 31.95×10^{-3} J m^{-2} which is obviously much less than the surface energy of water, 72.80×10^{-3} J m^{-2}.[69,70]

4.2 Cost analysis

To bring this nanostructure to market, cost can ultimately be the breaking point for its use by the general public. In terms of nanoparticle treatments, the materials used are often expensive (gold and silver) and here a discussion surrounding the cost of treatment *versus* the MIC is provided. Fig. 10a and b shows the cost of the nanoparticle treatment for Gram-positive and Gram-negative bacteria, respectively, for various material systems *versus* its MIC value. No distinction was made between shapes or sizes of the NPs. From this figure, it is evident that gold and silver nanoparticle treatments are the most expensive ones whatever the MIC value considered. Cheaper alternatives based on metal oxides like TiO_2, ZnO and Bi_2O_3 exist. Our Bi_2O_3 NF has been included in this analysis and was found to be very cost effective. This demonstrates that the metal oxide nanostructures produced in this work are a good alternative to noble metal nanoparticles for antibacterial applications.

5 Conclusions

Bi_2O_3 nano-flakes have been successfully synthesized by PLAL at high fluence (~160 J cm^{-2}) without any external assistance like acoustic, electric or magnetic fields. The nano-flakes exhibited two different phases: α- and γ- (commensurate structure). The physical dimensions of the flakes were around 1 μm along the *x*- and *y*-axis while only 47.0 ± 12.7 nm thick along the *z*-axis. The strongest advantage of using PLAL as a synthesis methodology is the cleanliness of the Bi_2O_3's surface. More work is required to finely tune the irradiation time, the fluence and the repetition rate in order to control more precisely the crystalline structure, and thickness of the Bi_2O_3 nano-flakes. The nano-flakes can also be used as cost-effective antibacterial agents against antibiotic resistant Gram-positive and -negative bacteria, as shown in this report against MSRA and MDR-EC. More work is required in order to fully understand the mechanism of action of the flake against the bacteria's membrane.

Conflicts of interest

There are no conflicts of interests to declare.

Acknowledgements

L. D. G., M. K., S. E. and G. G. would like to thank the Center for Integrative Nanotechnology Sciences (CINS) of UA Little Rock for the use of their UV-visible spectrometer, AFM, SEM and TEM. T. B. H. acknowledges the financial support from the National Science Foundation (NSF) (Grant #DMR-1709612). P. P. and A. P. thanks the Kleberg Advanced Microscopy Center at UTSA and DoD financing support #W911NF-18-1-0439.

References

1 ACSIHC Landmarks, *The discovery and development of penicillin*, ACS & RSC, 1999, available from http://www.acs.org/content/acs/en/education/whatischemistry/landmarks/flemingpenicillin.html.
2 R. I. Aminov, A Brief History of the Antibiotic Era: Lessons Learned and Challenges for the Future, *Front. Microbiol.*, 2010, **1**, 134.
3 WH Organization, available from https://www.who.int/antimicrobial-resistance/en/.

4 D. Berry, C. Xi and L. Raskin, Microbial ecology of drinking water distribution systems, *Curr. Opin. Biotechnol.*, 2006, **17**(3), 297–302.
5 J. P. Cabral, Water microbiology. Bacterial pathogens and water, *Int. J. Environ. Res. Public Health*, 2010, **7**(10), 3657–3703.
6 J. M. Schierholz and J. Beuth, Implant infections: a haven for opportunistic bacteria, *J. Hosp. Infect.*, 2001, **49**(2), 87–93.
7 L. D. Geoffrion and G. Guisbiers, Quantum confinement: size on the grill!, *J. Phys. Chem. Solids*, 2020, **140**, 109320.
8 G. Guisbiers, Advances in thermodynamic modelling of nanoparticles, *Adv. Phys.: X*, 2019, **4**(1), 1668299.
9 N. Elahi, M. Kamali and M. H. Baghersad, Recent biomedical applications of gold nanoparticles: a review, *Talanta*, 2018, **184**, 537–556.
10 C. Marambio-Jones and E. M. V. Hoek, A review of the antibacterial effects of silver nanomaterials and potential implications for human health and the environment, *J. Nanopart. Res.*, 2010, **12**(5), 1531–1551.
11 S. Kayal and R. V. Ramanujan, Anti-cancer drug loaded iron-gold core-shell nanoparticles (Fe@Au) for magnetic drug targeting, *J. Nanosci. Nanotechnol.*, 2010, **10**(9), 5527–5539.
12 J. Yin, S. Shan, L. Yang, D. Mott, O. Malis, V. Petkov, *et al.*, Gold–Copper Nanoparticles: Nanostructural Evolution and Bifunctional Catalytic Sites, *Chem. Mater.*, 2012, **24**(24), 4662–4674.
13 A. Magrez, S. Kasas, V. Salicio, N. Pasquier, J. W. Seo, M. Celio, *et al.*, Cellular toxicity of carbon-based nanomaterials, *Nano Lett.*, 2006, **6**(6), 1121–1125.
14 S. Dadashi, R. Poursalehi and H. H. Delavari, Formation, gradual oxidation mechanism and tunable optical properties of Bi/Bi_2O_3 nanoparticles prepared by Nd:YAG laser ablation in liquid: Dissolved oxygen as genesis of tractable oxidation, *Mater. Res. Bull.*, 2018, **97**, 421–427.
15 L. Escobar-Alarcon, E. V. Granados, D. A. Solis-Casados, O. Olea-Mejia, M. Espinosa-Pesqueira and E. Haro-Poniatowski, Preparation of bismuth-based nanosheets by ultrasound-assisted liquid laser ablation, *Appl. Phys. A: Mater. Sci. Process.*, 2016, **122**(4), 1–7.
16 M. A. Gondal, T. A. Saleh and Q. Drmosh, Optical Properties of Bismuth Oxide Nanoparticles Synthesized by Pulsed Laser Ablation in Liquids, *Sci. Adv. Mater.*, 2012, **4**(3–4), 507–510.
17 R. A. Ismail and F. A. Fadhil, Effect of electric field on the properties of bismuth oxide nanoparticles prepared by laser ablation in water, *J. Mater. Sci.: Mater. Electron.*, 2014, **25**(3), 1435–1440.
18 S. Jain, D. G. Hirst and J. M. O'Sullivan, Gold nanoparticles as novel agents for cancer therapy, *Br. J. Radiol.*, 2012, **85**(1010), 101–113.
19 B. Le Ouay and F. Stellacci, Antibacterial activity of silver nanoparticles: a surface science insight, *Nano Today*, 2015, **10**(3), 339–354.
20 Available from https://en.wikipedia.org/wiki/Prices_of_chemical_elements#cite_note-fn-transient-46.
21 L. D. Geoffrion, T. Hesabizadeh, D. Medina-Cruz, M. Kusper, P. Taylor, A. Vernet-Crua, *et al.*, Naked selenium nanoparticles for antibacterial and anticancer treatment, *ACS Omega*, 2020, **5**, 2660–2669.
22 B. Zare, M. A. Faramarzi, Z. Sepehrizadeh, M. Shakibaie, S. Rezaie and A. R. Shahverdi, Biosynthesis and recovery of rod-shaped tellurium nanoparticles and their bactericidal activities, *Mater. Res. Bull.*, 2012, **47**(11), 3719–3725.
23 S. Dadashi, R. Poursalehi and H. Delavari, Optical and structural properties of oxidation resistant colloidal bismuth/gold nanocomposite: an efficient nanoparticles based contrast agent for X-ray computed tomography, *J. Mol. Liq.*, 2018, **254**, 12–19.
24 S. Dadashi, R. Poursalehi and H. Delavari, Optical and structural properties of Bi-based nanoparticles prepared via pulsed Nd:YAG laser ablation in organic liquids, *Appl. Phys. A: Mater. Sci. Process.*, 2018, **124**(6), 406.
25 X. Yu, A. Li, C. Zhao, K. Yang, X. Chen and W. Li, Ultrasmall Semimetal Nanoparticles of Bismuth for Dual-Modal Computed Tomography/Photoacoustic Imaging and Synergistic Thermoradiotherapy, *ACS Nano*, 2017, **11**(4), 3990–4001.
26 G. Bandoli, D. Barreca, E. Brescacin, G. A. Rizzi and E. Tondello, Pure and mixed phase Bi_2O_3 thin films obtained by metal organic chemical vapor deposition, *Chem. Vap. Deposition*, 1996, **2**(6), 238–242.
27 C. Y. Pan, Y. Yan, H. D. Li and S. Hu, Synthesis of Bismuth Oxide Nanoparticles by a Templating Method and its Photocatalytic Performance, *Adv. Mater. Res.*, 2012, **557–559**, 615–618.
28 F. Farzaneh, L. Jafari Foruzin, Z. Sharif and E. Rashtizadeh, Green Synthesis and Characterization of Bi_2O_3 Nanorods as Catalyst for Aromatization of 1,4-Dihydropyridines, *J. Sci., Islamic Repub. Iran*, 2017, **28**, 113–118.
29 Y. Lu, Y. Zhao, J. Zhao, Y. Song, Z. Huang, F. Gao, *et al.*, Induced Aqueous Synthesis of Metastable β-Bi_2O_3 Microcrystals for Visible-Light Photocatalyst Study, *Cryst. Growth Des.*, 2015, **15**(3), 1031–1042.
30 H. Oudghiri-Hassani, S. Rakass, F. T. Al Wadaani, K. J. Al-ghamdi, A. Omer, M. Messali, *et al.*, Synthesis, characterization and photocatalytic activity of α-Bi_2O_3 nanoparticles, *Journal of Taibah University for Science*, 2018, **9**(4), 508–512.
31 M. Schlesinger, M. Weber, S. Schulze, M. Hietschold and M. Mehring, Metastable beta-Bi_2O_3 Nanoparticles with Potential for Photocatalytic Water Purification Using Visible Light Irradiation, *ChemistryOpen*, 2013, **2**(4), 146–155.
32 A. Hameed, T. Montini, V. Gombac and P. Fornasiero, Surface phases and photocatalytic activity correlation of Bi_2O_3/Bi_2O_{4-x} nanocomposite, *J. Am. Chem. Soc.*, 2008, **130**(30), 9658–9659.
33 C. Stewart, K. Konstantinov, S. McKinnon, S. Guatelli, M. Lerch, A. Rosenfeld, *et al.*, First proof of bismuth oxide nanoparticles as efficient radiosensitisers on highly radioresistant cancer cells, *Phys. Med.*, 2016, **32**(11), 1444–1452.
34 K. Bogusz, M. Tehei, C. Stewart, M. McDonald, D. Cardillo, M. Lerch, *et al.*, Synthesis of potential theranostic system

consisting of methotrexate-immobilized (3-aminopropyl) trimethoxysilane coated α-Bi_2O_3 nanoparticles for cancer treatment, *RSC Adv.*, 2014, **4**(46), 24412–24419.

35 Y. Shimizu, E. Kanazawa, Y. Takao and M. Egashira, H_2 Sensing Properties of Metal Oxide Semiconductors as Varistor-Type Gas Sensors, *IEEJ Transactions on Sensors and Micromachines*, 1997, **117**(11), 560–564.

36 M. R. Ambika, N. Nagaiah and S. K. Suman, Role of bismuth oxide as a reinforcer on gamma shielding ability of unsaturated polyester based polymer composites, *J. Appl. Polym. Sci.*, 2017, **134**(13), 44657.

37 C. Stewart, K. Konstantinov, M. McDonald, K. Bogusz, D. Cardillo, S. Oktaria, *et al.*, Engineering of Bismuth Oxide Nanoparticles to Induce Differential Biochemical Activity in Malignant and Nonmalignant Cells, *Part. Part. Syst. Charact.*, 2014, **31**(9), 960–964.

38 A. J. Salazar-Pérez, M. A. Camacho-López, R. A. Morales-Luckie, V. Sánchez-Mendieta, F. Ureña-Núñez and J. Arenas-Alatorre, Structural evolution of Bi_2O_3 prepared by thermal oxidation of bismuth nano-particles, *Sociedad Mexicana de Ciencia y Tecnología de Superficies y Materiales*, 2005, **18**, 4–8.

39 F. I. Lopez-Salinas, G. A. Martinez-Castanon, J. R. Martinez-Mendoza and F. Ruiz, Synthesis and characterization of nanostructured powders of Bi2O3, BiOCl and Bi, *Mater. Lett.*, 2010, **64**(14), 1555–1558.

40 H. Kodama, A. Watanabe and Y. Yajima, Synthesis of a new bismuth oxide fluoride with the γ-Bi_2O_3 structure type, *J. Solid State Chem.*, 1987, **67**(1), 170–175.

41 D. S. Aidhy, J. C. Nino, S. B. Sinnott, E. D. Wachsman and S. R. Phillpot, Vacancy-Ordered Structure of Cubic Bismuth Oxide from Simulation and Crystallographic Analysis, *J. Am. Ceram. Soc.*, 2008, **91**(7), 2349–2356.

42 N. Cornei, N. Tancret, F. Abraham and O. Mentre, New epsilon-Bi_2O_3 metastable polymorph, *Inorg. Chem.*, 2006, **45**(13), 4886–4888.

43 A. F. Gualtieri, S. Immovilli and M. Prudenziati, Powder X-ray diffraction data for the new polymorphic compound ω-Bi_2O_3, *Powder Diffr.*, 2013, **12**(02), 90–92.

44 H. T. Fan, X. M. Teng, S. S. Pan, C. Ye, G. H. Li and L. D. Zhang, Optical properties of δ-Bi_2O_3 thin films grown by reactive sputtering, *Appl. Phys. Lett.*, 2005, **87**(23), 231916.

45 Y. Qiu, D. Liu, J. Yang and S. Yang, Controlled Synthesis of Bismuth Oxide Nanowires by an Oxidative Metal Vapor Transport Deposition Technique, *Adv. Mater.*, 2006, **18**(19), 2604–2608.

46 M. Anilkumar, R. Pasricha and V. Ravi, Synthesis of bismuth oxide nanoparticles by citrate gel method, *Ceram. Int.*, 2005, **31**(6), 889–891.

47 C. Y. Pan, X. H. Li, F. Wang and L. F. Wang, Synthesis of bismuth oxide nanoparticles by the polyacrylamide gel route, *Ceram. Int.*, 2008, **34**(2), 439–441.

48 R. K. Jha, R. Pasricha and V. Ravi, Synthesis of bismuth oxide nanoparticles using bismuth nitrate and urea, *Ceram. Int.*, 2005, **31**(3), 495–497.

49 B. Gökce, V. Amendola and S. Barcikowski, Opportunities and Challenges for Laser Synthesis of Colloids, *ChemPhysChem*, 2017, **18**, 983–985.

50 D. Zhang, B. Gokce and S. Barcikowski, Laser Synthesis and Processing of Colloids: Fundamentals and Applications, *Chem. Rev.*, 2017, **117**(5), 3990–4103.

51 M. Flores-Castaneda, E. Camps, M. Camacho-Lopez, S. Muhl, E. Garcia and M. Figueroa, Bismuth nanoparticles synthesized by laser ablation in lubricant oils for tribological tests, *J. Alloys Compd.*, 2015, **643**, S67–S70.

52 R. G. T. Rosa, C. D. Duarte, W. H. Schreiner, N. P. Mattoso, A. G. Bezerra, A. Barison, *et al.*, Structural, morphological and optical properties of Bi NPs obtained by laser ablation and their selective detection of L-cysteine, *Colloids Surf., A*, 2014, **457**, 368–373.

53 R. K. Verma, K. Kumar and S. B. Rai, Near infrared induced optical heating in laser ablated Bi quantum dots, *J. Colloid Interface Sci.*, 2013, **390**, 11–16.

54 D. Zhang, B. Gökce and S. Barcikowski, Laser Synthesis and Processing of Colloids: Fundamentals and Applications, *Chem. Rev.*, 2017, **117**, 3990–4103.

55 M. Kusper and G. Guisbiers, Synthesis of aluminum oxide nanoparticles by laser ablation in liquids, *MRS Adv.*, 2018, **3**(64), 3899–3903.

56 O. Van Overschelde and G. Guisbiers, Photo-fragmentation of selenium powder by Excimer laser ablation in liquids, *Opt. Laser Technol.*, 2015, **73**, 156–161.

57 Q. Zhang, Y. Zhou, F. Wang, F. Dong, W. Li, H. M. Li, *et al.*, From semiconductors to semimetals: bismuth as a photocatalyst for NO oxidation in air, *J. Mater. Chem. A*, 2014, **2**(29), 11065–11072.

58 C.-H. Ho, C.-H. Chan, Y.-S. Huang, L.-C. Tien and L.-C. Chao, The study of optical band edge property of bismuth oxide nanowires α-Bi_2O_3, *Opt. Express*, 2013, **21**, 11965–11972.

59 K. Balasubramanian, R. Udayabhaskar and A. Kishore, Optical and phonon properties of Sm-doped α-BiO micro rods, *Appl. Phys. A: Mater. Sci. Process.*, 2014, **117**, 1409–1414.

60 C. H. Ho, C. H. Chan, Y. S. Huang, L. C. Tien and L. C. Chao, The study of optical band edge property of bismuth oxide nanowires alpha-Bi_2O_3, *Opt. Express*, 2013, **21**(10), 11965–11972.

61 Á. R. Landa-Cánovas, E. Vila, J. Hernández-Velasco, J. Galy and A. Castro, Transmission Electron Microscopy Study of Low Mo-content Bi–Mo–O Phases, *Microsc. Microanal.*, 2012, **18**, 71–72.

62 W. Zhou, D. A. Jefferson, M. Alario-Franco and J. M. Thomas, Superlattices in ternary oxides derived from bismuth oxide (Bi_2O_3): new families of ordered phases based on the fluorite structure, *J. Phys. Chem.*, 1987, **91**, 512–514.

63 P. A. Doyle and P. S. Turner, Relativistic Hartree–Fock X-ray and electron scattering factors, *Acta Crystallogr., Sect. A: Cryst. Phys., Diffr., Theor. Gen. Crystallogr.*, 1968, **A24**, 390–397.

64 V. Campos, A. Almaguer-Flores, D. Velasco-Aria, D. Diaz and S. E. Rodil, Bismuth and Silver Nanoparticles as Antimicrobial Agent over Subgingival Bacterial and Nosocomial Strains, *J. Mater. Sci. Eng. A*, 2018, **8**, 142–146.

65 Y. Luo, M. Hossain, C. Wang, Y. Qiao, J. An, L. Ma, *et al.*, Targeted nanoparticles for enhanced X-ray radiation killing of multidrug-resistant bacteria, *Nanoscale*, 2013, **5**, 687–694.
66 H. Ma, Z. Shen and S. Ben, Understanding the exfoliation and dispersion of MoS_2 nanosheets in pure water, *J. Colloid Interface Sci.*, 2018, **517**, 204–212.
67 A. M. Müller, Optical control of layered nanomaterial generation by pulsed-laser ablation in liquids, *J. Mod. Opt.*, 2020, **67**, 49–54.
68 G. Guisbiers and M. José-Yacaman, Use of Chemical Functionalities to Control Stability of Nanoparticles, *Reference Module in Chemistry, Molecular Sciences and Chemical Engineering*, 2018, Encyclopedia of Interfacial Chemistry, pp. 875–885.
69 F. M. Tezel and İ. Afşin Kariper, Synthesis, surface tension, optical and dielectric properties of bismuth oxide thin film, *Mater. Sci.-Pol.*, 2017, **35**(1), 87–93.
70 G. Guenther, R. Theissmann and O. Guillon, Size-Dependent Phase Transformations in Bismuth Oxide Nanoparticles. II. Melting and Stability Diagram, *J. Phys. Chem. C*, 2014, **118**(46), 27020–27027.
71 Y. N. Slavin, J. Asnis, U. O. Hafeli and H. Bach, Metal nanoparticles: understanding the mechanisms behind antibacterial activity, *J. Nanobiotechnol.*, 2017, **15**(1), 65.
72 S. A. Moreno-Álvarez, G. A. Martínez-Castañón, N. Niño-Martínez, J. F. Reyes-Macías, N. Patiño-Marín, J. P. Loyola-Rodríguez, *et al.*, Preparation and bactericide activity of gallic acid stabilized gold nanoparticles, *J. Nanopart. Res.*, 2010, **12**(8), 2741–2746.
73 M. Valodkar, S. Modi, A. Pal and S. Thakore, Synthesis and anti-bacterial activity of Cu, Ag and Cu–Ag alloy nanoparticles: a green approach, *Mater. Res. Bull.*, 2011, **46**(3), 384–389.
74 M. Ahamed, H. A. Alhadlaq, M. A. M. Khan, P. Karuppiah and N. A. Al-Dhabi, Synthesis, Characterization, and Antimicrobial Activity of Copper Oxide Nanoparticles, *J. Nanomater.*, 2014, **2014**, 1–4.
75 A. Azam, A. S. Ahmed, M. Oves, M. S. Khan and A. Memic, Size-dependent antimicrobial properties of CuO nanoparticles against Gram-positive and -negative bacterial strains, *Int. J. Nanomed.*, 2012, **7**, 3527–3535.
76 V. V. Thekkae Padil and M. Cernik, Green synthesis of copper oxide nanoparticles using gum karaya as a biotemplate and their antibacterial application, *Int. J. Nanomed.*, 2013, **8**, 889–898.
77 S. Siddique, Z. H. Shah, S. Shahid and F. Yasmin, Preparation, characterization and antibacterial activity of ZnO nanoparticles on broad spectrum of microorganisms, *Acta Chim. Slov.*, 2013, **60**(3), 660–665.
78 E.-K. Zarrindokht, Antibacterial activity of ZnO nanoparticle on Gram-positive and Gram-negative bacteria, *Afr. J. Microbiol. Res.*, 2012, **5**(12), 1368–1373.
79 E. Zonaro, S. Lampis, R. J. Turner, S. J. Qazi and G. Vallini, Biogenic selenium and tellurium nanoparticles synthesized by environmental microbial isolates efficaciously inhibit bacterial planktonic cultures and biofilms, *Front. Microbiol.*, 2015, **6**, 584.